

Resistor Network Modeling of Conductive Domain Walls in Lithium Niobate

Benjamin Wolba,* Jan Seidel, Claudio Cazorla, Christian Godau, Alexander Haußmann, and Lukas M. Eng

Here the concept of a 2D resistor network (2D RN) is applied in order to model the electrical conductivity along sheet-like domain walls (DWs) in single crystalline lithium niobate (sc-LNO). The only input to the RN modeling approach is the DW inclination angle distribution, as measured previously with respect to the polar c -axis. The simulations then show that a 2D network of Ohmic resistors not only adequately accounts for the different boundary conditions envisaged in experiments, but equally well provides a direct link between the local domain wall conductivity (DWC) and the DW inclination angle α . Moreover, the RN simulations can be directly compared to local-scale transport measurements, as obtained by scanning probe techniques. The conceptual simplicity and the low computational effort make the present RN modeling approach a useful tool for both the advanced interpretation and evaluation of potential DWC ferroelectrics.

1. Introduction

Domain walls (DWs) in ferroelectrics are topological defects that penetrate across the full bulk material, while separating regions of different dielectric polarization.^[1] Although DWs measure just a few unit cells in width^[2–5] they exhibit completely different physical properties as compared to the material's bulk,^[6] such as altered dielectric,^[7] optical,^[8] magnetic,^[9] and also conductive properties. DWs thus are very promising candidates for both the bottom-up assembly of functional nanoelectronic

devices,^[10] and the fundamental inspection by theory and experiment.

While ferroelectrics constitute wide-band gap semiconductors with good insulating properties, their DWs may possess a significantly increased electrical conductivity, as is of central focus in the work here. This so-called domain wall conductivity (DWC) has been reported first for multiferroic bismuth ferrite^[11] and lead-zirconate-titanate^[12] thin films, followed by research on (improper) erbium manganite^[13] and barium titanate^[14] bulk ferroelectric crystals. DWC in lithium niobate (LiNbO₃:LNO) so far was reported to happen under photoexcitation only.^[15,16] However, recent experiments by Godau et al.^[17] on LNO single crystals (sc) have


shown that reshaping the DW to larger inclination angles by applying a dedicated electrical tuning protocol enhances DWC by 3–4 orders of magnitude, and gives rise to DW currents in the upper μ A range at room temperature and in the dark.

Theoretical approaches applied to explain the increased DWC in these materials include phenomenological Landau^[18] and Landau–Ginzburg–Devonshire theory,^[19] and more recently also the combination of quantum mechanics with phenomenological Landau theory.^[20] All these microscopic theories aim at predicting and quantifying the relevant local-scale domain wall parameters, i.e., the DW formation energy, the free charge distribution, and the DW conductivity. Nevertheless, it is difficult to compare the outcomes of such microscopic theories directly to experimental data, as the latter generally is based on macroscopic quantities. In contrast, our resistor network (RN) approach provides a clue link to experiments, in spite of being nonpredictive (i.e., as it requires some initial experimental input). Hence, our results can be directly compared to the local currents flowing within the DW as measured for instance by conductive atomic force microscopy (cAFM). The simple picture of a RN thus elegantly complements the microscopic theories of DWC.

2. Methods

For the modeling a 2D network of linear, Ohmic resistors (see **Figure 1a**) was used, that was carefully crafted on the basis of the DW's inclination angle distribution. Resistor networks (RN) have already been applied impressively for modeling a

B. Wolba
 Institute of Theoretical Physics
 Technische Universität Dresden
 Germany
 E-mail: benjamin.wolba1@tu-dresden.de
 B. Wolba, C. Godau, Dr. A. Haußmann, Prof. L. M. Eng
 Institute of Applied Physics
 Technische Universität Dresden
 01062 Dresden, Germany
 B. Wolba, Prof. J. Seidel, Dr. C. Cazorla
 School of Materials Science and Engineering
 University of New South Wales
 NSW 2052 Kensington, Australia
 Dr. A. Haußmann, Prof. L. M. Eng
 cfaed – Center For Advancing Electronics Dresden
 Technische Universität Dresden
 Germany

 The ORCID identification number(s) for the author(s) of this article can be found under <https://doi.org/10.1002/aelm.201700242>.

DOI: 10.1002/aelm.201700242

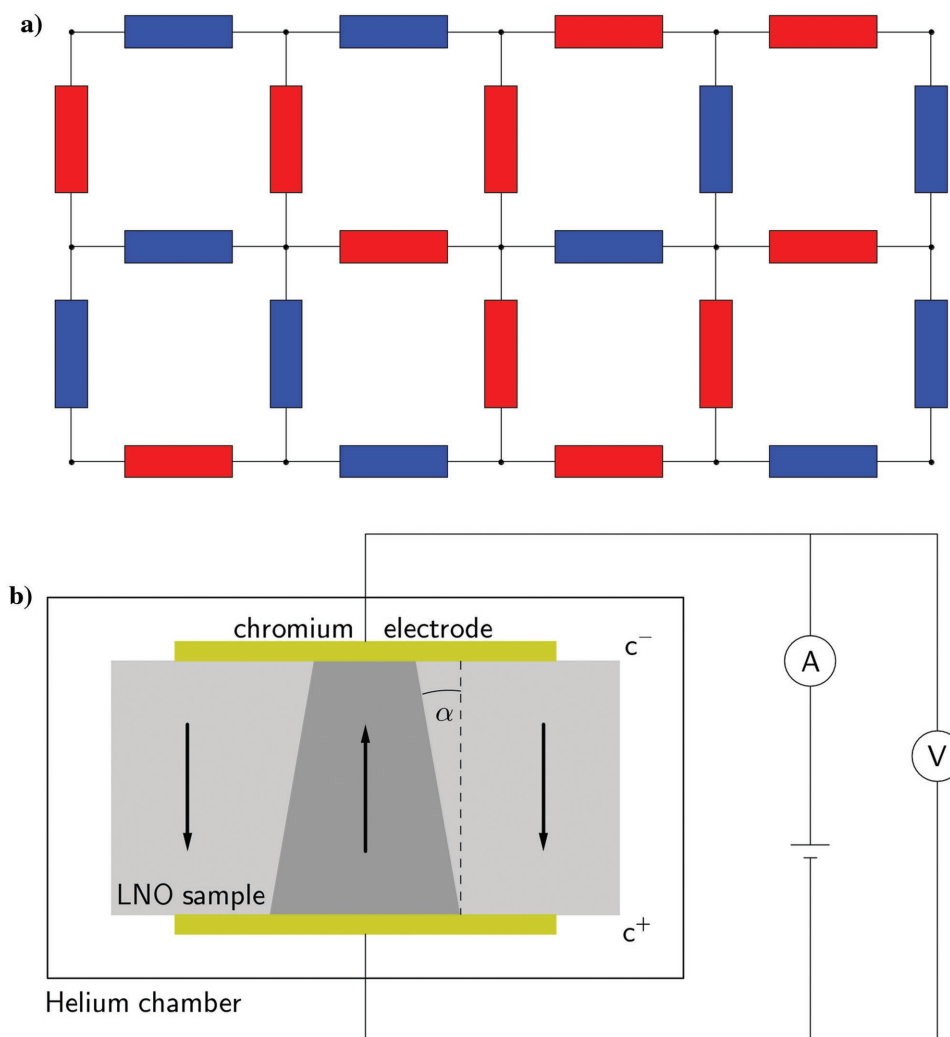


Figure 1. a) Sketch of a square-lattice resistor network, with different resistive values shown color coded in red and blue. b) Experimental setup as applied for inducing bent domain walls (DWs) into single crystalline lithium niobate (sc-LNO) samples that possess large inclination angles α (see ref. [17]). The setup also shows how to extract the domain wall conductivity (DWC) by experiment.

broad variety of different electronic transport scenarios, such as topological Kondo-Insulators,^[21] manganite thin films upon Mott phase transitions,^[22] as well as the currents flowing in disordered semiconductors,^[23] in composite materials,^[24] or in low-dimensional nanostructures^[25] like graphene^[26] or single-stranded DNA molecules.^[27]

The 2D-RN-DWC-modeling used the 3D distribution of inclination angles α of one single DW as an input, as measured by Godau et al.^[17] [see Figure 1b]. Details on how to prepare and analyze such a single, highly conductive DW can be found in refs. [17,28,29]. In brief, the Godau work provided a reliable protocol of how to increase the tilt angles α in sc-LNO samples; applying a moderate electrical field of $\approx 60\%$ of the coercive field across the $200\ \mu\text{m}$ thick sample tunes a DW with a diameter in the range of $50\ \mu\text{m}$ to larger bending angles with respect to the sample c -axis, hence increasing the DWC. The key technique in the Godau work, used to quantify the local inclination angle α both before and after electric field

tuning, was Cerenkov second-harmonic generation (CSHG) microscopy.^[30,31]

In the present work, these two data sets of DW inclination angles (before and after sample tuning) were used as the input for the RN modeling. First, the raw data from Godau et al. was interpolated on a regular square lattice of $(2 \cdot N) \times N$ lattice points. For simplicity all simulations presented in this work were carried out on a square lattice; a hexagonal lattice was tested as well for comparison reasons yielding the same results for sufficiently large N . The result of the $N = 200$ interpolation is illustrated in **Figure 2a,b** before and after DWC tuning, respectively. The distribution of angles α at every point in $z - \varphi$ -space is shown color-coded, with red and blue colors indicating head-to-head (h2h) and tail-to-tail (t2t) DW configurations, respectively. h2h DWs provided a DW conductivity that was at least one order of magnitude larger as compared to t2t DWs.^[19] The data in Figure 2a,b is displayed in a so-called “developed” or “world-map” view, unrolling the quasi hexagonal

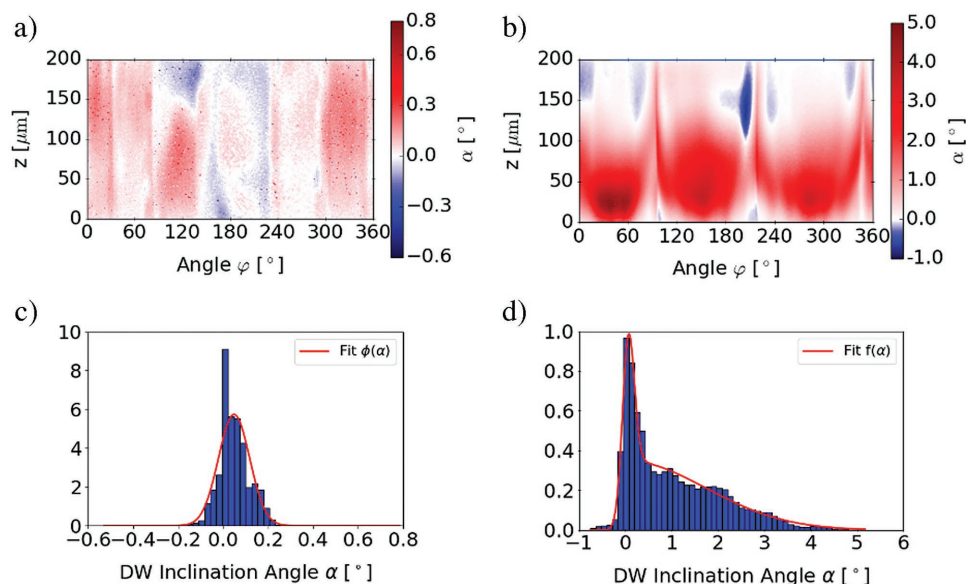


Figure 2. Distribution of DW inclination angles α a) before and b) after DWC enhancement, interpolated onto a 400×200 lattice in cylindrical $z - \varphi$ -coordinates, and displayed in a so-called “world-map” (data from ref. [17]); c,d) The histograms thereof before and after tuning, respectively. (c) matches to a single normal distribution, while (d) is fitted to an asymmetric superposition of a normal and a skewed normal distribution.

domain wall rim (φ -axis) along the x -axis. Furthermore, inclination angles α covered a range of $[-0.5^\circ, \dots, +0.8^\circ]$ “before” DWC tuning only, while being dramatically increased to $[-1^\circ, \dots, +5^\circ]$ “after” applying the electric field tuning procedure.

Next, the distribution of DW inclination angles α (Figure 2a,b) was statistically analyzed by the two histograms illustrated in Figure 2c,d. The α -distribution before tuning (Figure 2c) adequately matched a simple normal distribution $\phi(\alpha) = \frac{1}{\sqrt{2 \cdot \pi \cdot \sigma^2}} \cdot e^{-\frac{(\alpha-\mu)^2}{2\sigma^2}}$. The histogram after tuning

(Figure 2d) was approximated through an asymmetric superposition $f(\alpha) = p \cdot \phi(\alpha) + (1 - p) \cdot s(\alpha)$ using a single normal distribution $\phi(\alpha)$ and a skewed normal distribution $s(\alpha) = 2 \cdot \phi(\alpha) \cdot \Phi(a \cdot \alpha)$,^[32] where $\Phi(\alpha) = \int_{-\infty}^{\alpha} \phi(t) \cdot dt = \frac{1}{2} \left[1 + \operatorname{erf} \left(\frac{\alpha - \mu}{\sqrt{2} \cdot \sigma} \right) \right]$ is representing the cumulative normal distribution, a the skewness, and p the amount of asymmetry.

The sample tuning procedure affected the DW inclination in the three following ways as deduced from the histogram fitting: shifting the mean value to larger inclination angles; increasing the variance; and finally, skewing the normal distribution. Notably, not the whole distribution seemed to be affected by the sample tuning, since a large peak centered around $\alpha = 0^\circ$ remained (see Figure 2d). Such an asymmetric histogram could be matched by the superposition of a skewed normal distribution that arose due to sample tuning, and a single normal distribution reflecting the nondisturbed DW inclinations. As seen from **Table 1**, the single normal distribution had the same mean value as did the simple normal fit before DW tuning, notably with an increased variance.

Finally, the interpolated data (Figure 2a,b) was linked to the RN formalism, as electrical transport along the DW in Figure 1b was modeled by a RN on a square lattice as sketched in Figure 1a for the $(2 \cdot N) \times N$ resistor array. Importantly,

the conductivity of each resistor was determined by the local DW inclination angle α at the corresponding lattice site. This assumption was well justified both by theory and experiment^[15,19] showing that the local conductivity at every lattice point behaves as

$$\sigma = \sigma_0 \cdot \sin(\alpha) \quad (1)$$

with σ_0 being a proportionality constant. Theoretical calculations for uniaxial ferroelectrics such as lithium niobate using the Landau–Ginzburg–Devonshire theory had shown that the conductivity of holes in the tail-to-tail (t2t) regions was at least one order of magnitude lower as compared to the h2h DW.^[19] This was due to both the lower concentration and the lower mobility of holes at the DW. Hence, the proportionality constant σ_0 in t2t (blue) areas was set 10 times smaller in our calculations here, as compared to h2h DWs: $\sigma_{\text{hole}} = \sigma_0/10 \cdot |\sin(\alpha)|$, while highly conductive h2h (red) areas were governed by $\sigma_{\text{electron}} = \sigma_0 \cdot |\sin(\alpha)|$. The factor of “10” could be viewed as an upper limit for hole conductivity. Note, that holes and electrons specified here the majority charge-carrier type for electrical transport in t2t and h2h DWs, respectively. In the following, all data was displayed in a normalized fashion as ρ_i/σ_0^{-1} or σ_i/σ_0 .

Table 1. Fit parameters for modeling the inclination angle histograms by means of normal and skewed normal distributions.

	Mean μ [°]	SD σ [°]	Skewness a	Asymmetry p
Before tuning				
$\phi(\alpha)$	0.05	0.07		
After tuning				
$p \cdot \phi(\alpha)$	0.05	0.14		0.24
$s(a \cdot \alpha)$	0.79	1.74	18.2	

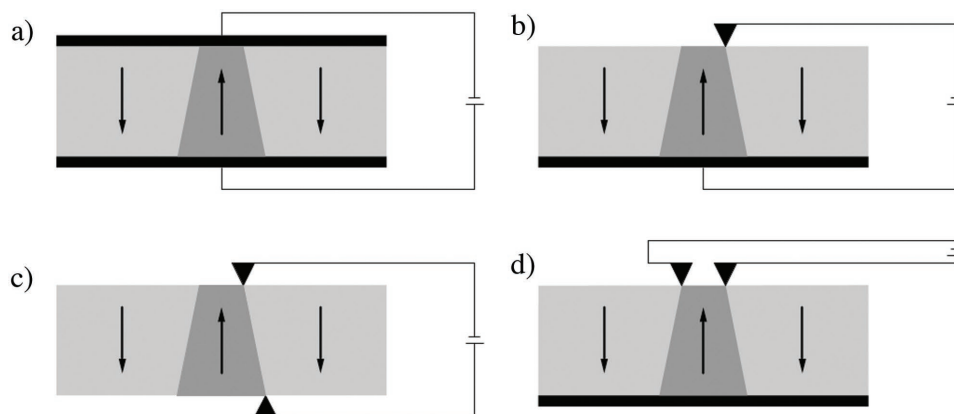


Figure 3. Sketch of the different scenarios used for modeling the conductive DW in a resistor network: a) plate-to-plate (pp), b) tip-to-plate (tp), and c,d) tip-to-tip (tt) boundary conditions. Note that (a) and (b) reflect exactly the two setups as experimentally used by Godau et al.^[17] Cases (c) and (d) might provide novel insights into DWC, since modeling electrical transport both perpendicular and parallel to the sample surface and are given for completeness and as inspiration for future work.

In order to solve the Kirchhoff equations of the resulting RN, a numerical approach based on the Gauss–Seidel relaxation method was chosen to be applied.^[33] The potential distribution in a resistor network was a harmonic function; hence the potential at a specific node is given by the suitably weighted average of the potentials at neighboring nodes (nearest neighbors, NN)

$$V(\vec{r}) = \frac{\sum_{NN} \sigma_{\vec{r}\vec{r}'} V(\vec{r}')}{\sum_{NN} \sigma_{\vec{r}\vec{r}'}} \quad (2)$$

where \vec{r} indicates the nodes' positions and $\sigma_{\vec{r}\vec{r}'}$ the conductivity of the resistor that connects to the neighboring nodes \vec{r} and \vec{r}' . The potential $V(\vec{r})$ was defined as the negative electrical potential $\phi_e(\vec{r})$. Starting with an initial potential distribution $V_0(\vec{r})$, the relation above was applied to every such node in order to calculate the next updated potential matrix. Cyclic iteration then allowed the potential distribution to converge towards the correct potential distribution. The calculation was stopped as soon as the maximal difference between two consecutive potential matrices falls below a certain threshold given as $\max(|V_{i+1}(\vec{r}) - V_i(\vec{r})|) < \epsilon$. The number of relaxation steps was stored in the so-called “counter” n . This solution method turned out to be especially beneficial for larger matrices as compared to the exact matrix solution of the corresponding linear network equations.

Solutions of the RN equations depended on the given boundary conditions, that corresponded to different experimental scenarios, as sketched in **Figure 3**. While periodic boundary conditions were applied along the φ -axis (reflecting the in-plane DW symmetry), the electrical potential had a fixed value at the upper c^+ and lower c^- LNO surface (along the z -axis). The study differentiated between the following three cases (see Figure 3):

- Plate-to-plate (pp) boundary condition (Figure 3a): the top and bottom electrode/interfaces were connected to a fixed potential of V_c and zero, respectively. This corresponded to the well-known plate capacitor setup, as for instance used for

macroscopic I–U recordings by Godau et al.^[17]. The plate-to-plate resistivity will be referred to as the total network resistivity.

- Tip-to-plate (tp) boundary condition (Figure 3b): the potential was fixed to V_c at one single node at the samples top surface, and was set to zero at the extended bottom contact. This scenario corresponded to local-scale cAFM measurements where a sharp conductive AFM-tip was used as the top electrode for monitoring the local I–U behavior.
- Tip-to-tip (tt) boundary condition (Figure 3c,d): Two different nodes were addressed locally by two independent tips, placed either on opposite surfaces (c) or at the same sample surface (d). The potential was fixed to zero at one node and to V_c at the other one. This scenario accounted for the two-point resistivity measurements using for instance two separate AFM-tips or two single point contacts (needles). The two setups provided orthogonal information on the transport properties, with (c) and (d) shedding light on the through-DW transport and the spurious sample surface conductivity, respectively.

Note that only cases (a) and (b) are treated in this paper, because they match to the experiments of Godau et al.^[17]

For these two cases (a) and (b), a linear potential drop across the sample was assumed, with the potential distribution normalized to the arbitrary value $V_c = 10$. In order to choose appropriate numerical parameters, the stability of the model was firstly evaluated by checking against several parameters while using the dataset of the DW after tuning.

At first, the effect of the lattice size (interpolation) on the total network resistivity was inspected (see **Figure 4a**) using the plate-to-plate boundary condition. As seen, the counter was analyzed in parallel (Figure 4b), reflecting the computational effort in order to relax the potential distribution below an error of $\epsilon = 10^{-8}$. For small lattice sizes N ($N < 100$), the total network resistivity always had a too low value (as compared to $N \rightarrow \infty$) and did not converge, since the interpolation of the DW inclination angle distribution inherently was too rough. For $N \geq 150$, a much more stable total network resistivity emerged, showing a clear trend towards saturation.

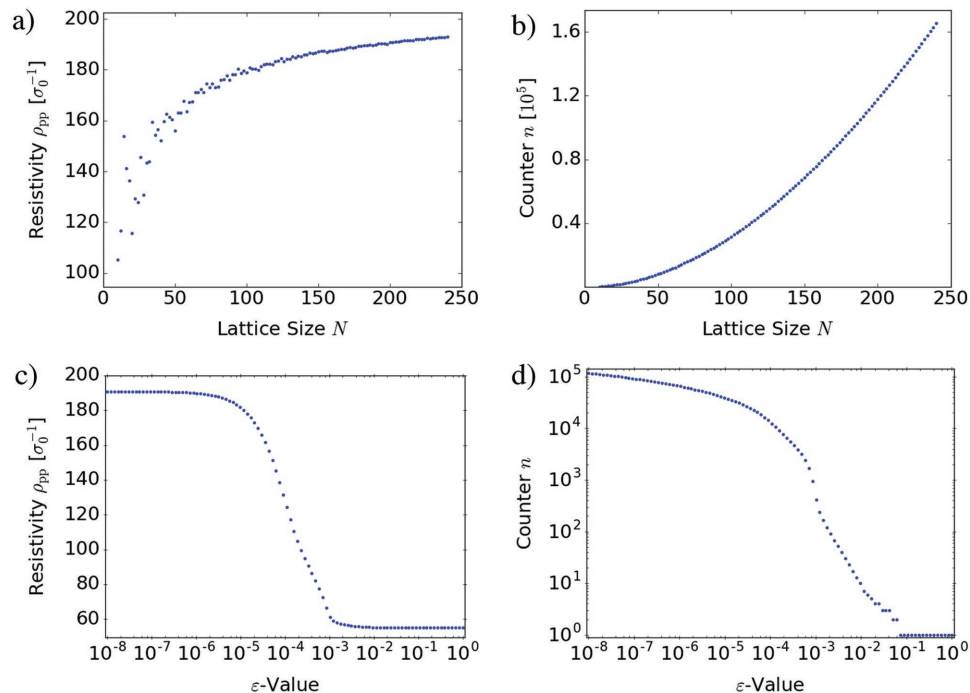


Figure 4. Stability analysis of the RN approach in the plate-to-plate configuration: Dependence of a) the total network resistivity ρ_{pp} , and b) the counter n as a function of lattice size N . (c) and (d) illustrate how the total network resistivity ρ_{pp} and the counter n depend on ϵ , respectively.

Meanwhile, the counter increased quadratically as expected for a square lattice. For larger N , not only the computational effort but also the required storage capacity for the matrix became demanding. As a compromise between accuracy in the total network resistivity and both computational effort and storage capacity, an optimal lattice size of $N = 200$ was chosen for the calculations to follow.

This means physically that $N = 200$ allowed a consistent modeling of the DWs conductivity as given by the diffraction-limited inclination data. A denser numerical grid did not improve the accuracy any more and higher resolved experimental data would be needed to go beyond that, which is not yet possible to get with state-of-the-art techniques.

Next, the dependence of both the total network resistivity and counter n on the ϵ -value was investigated for the same plate-to-plate setup and again for the DW inclination angle data after tuning. The results are displayed in Figure 4c,d.

Whenever ϵ had a large value ranging between 10^{-2} and 10^0 , only very few iterations were needed in order to terminate the recursion. The total network resistivity showed an almost constant but low value in this regime, that corresponded to the linear potential drop across the DW. For $10^{-5} < \epsilon < 10^{-2}$, both the counter and total network resistivity increased drastically. The initially linear potential distribution adapted to the effective potential distribution as governed by the resistor network in the plate-to-plate setup. Finally, around $\epsilon = 10^{-5}$, the counter increased much slower while the total network resistivity already exhibited clear saturation and convergence. It was manifested that an $\epsilon < 10^{-5}$ provided a very satisfying result, with the total network resistivity being almost constant here, and the counter increased only moderately.

3. Results and Discussion

For the parameters $N = 200$ and $\epsilon = 10^{-8}$, the network resistivity was now calculated in both the plate-to-plate and tip-to-plate configuration. In Figure 5 the potential drop both before (a,b) and after sample tuning (c,d) for the two cases is plotted, and the corresponding network resistivities are listed in Table 2. For the tp-case, we positioned the conductive tip as example at node 70 (i.e., at angle $\varphi = 126^\circ$) as clearly seen from the potential distributions in Figure 5b,d. The tip can equally be moved also to any other such node.

For the pp-boundary condition, the potential distribution prior to tuning (Figure 5a) mostly follows a linear potential drop along the z -direction, especially around $\varphi = 0^\circ$, where h2h-areas are penetrating across the whole LNO crystal thickness. For $80^\circ < \varphi < 240^\circ$, the potential distribution is heavily disturbed due to the presence of t2t DWs. After sample tuning (see Figure 5c) the potential nearly drops by 100% between 200 and 150 μm due to the t2t-areas (larger inclination angles, little amount of h2h DWs) and stays then nearly constant, manifesting in a metallic-like transport behavior.

In the tp-case (Figure 5b,d), the electrical potential always decays radially away from the biased tip, both laterally and into the depth of the sc-LNO sample. The decay length measures $\approx 50 \mu\text{m}$. This distribution is also affected by the t2t-regions, although they are not seen well in these pictures.

The overall value of the network resistivity in the tp-setup strongly depends on the position where the conductive tip has been positioned. We therefore calculated a position-dependent resistivity spectrum for both the DW state before and after sample tuning. This corresponds to scanning the tip over the

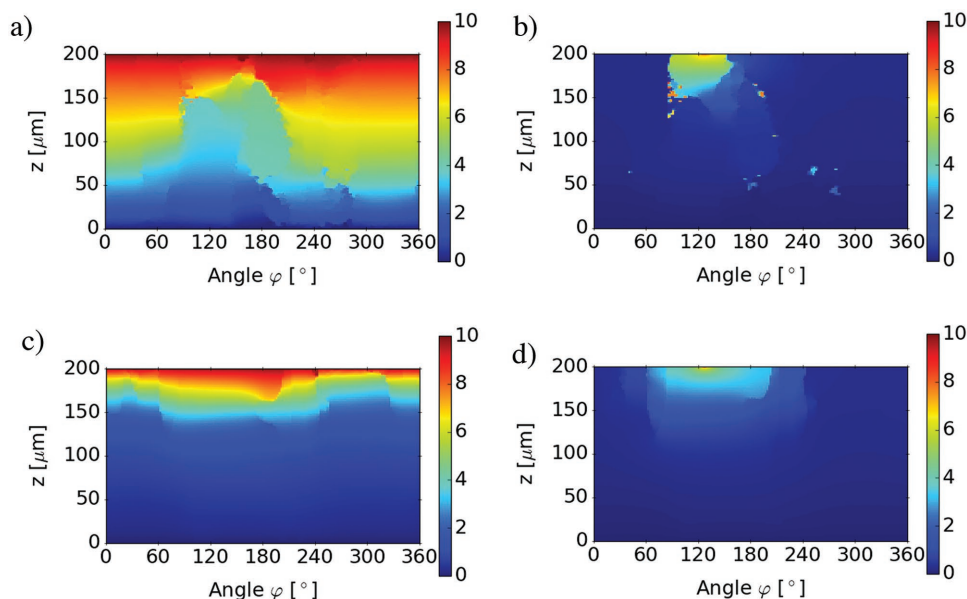


Figure 5. Potential distributions within the domain wall displayed in φ - z -space and normalized to the dimensionless value $V_c = 10$. Two boundary conditions are shown which are the plate-to-plate a,c) and the tip-to-plate b,d) scenarios, illustrated before a,b) and after c,d) sample tuning, respectively. In the tp-case, the tip contact point was positioned at an angle of 126° (node 70).

whole φ -range from 0° to 360° along the domain wall rim in the real experiment. The resulting spectra are shown in **Figure 6**.

While the network resistivity varies by five orders of magnitude before sample tuning, it varies only by two orders of magnitude after DW tuning in the tip-to-plate setup. This might be due to a larger fraction of DW inclination angles close to zero before DW tuning. Also before sample tuning, the corners of the hexagonally-shaped domain (see **Figure 2a**) are reflected by high-resistivity peaks at angles 34° , 88° , 156° , 227° , 289° , and 355° in the spectrum in **Figure 6a**, representing the border either between different h2h-areas or between a h2h- and t2t-area. The inclination angles at the DWs corners are decreased. Electronic transport happens mostly along the rim of the DW. By contrast after DW tuning the minima around 94° , 219° , and 347° correspond to the corners of the triangular DW (see **Figure 2b**). Due to the DW tuning, the DW inclination angles at the corners are severely increased, forming conducting channels through the DW. Generally the tip-plate resistivity is decreased by DW tuning in the range $80^\circ < \varphi < 240^\circ$.

The tip-to-plate conductivity spectrum, obtained from the inverse of the network resistivity, can be compared with the results of local probe cAFM-measurements, as conducted by Godau et al.^[17] for the DW state after sample tuning. In **Figure 7a**, the measured current (right axis) that was extracted from a cAFM-scan, is plotted in comparison to the calculated

tip-to-plate-network conductivity spectrum (left axis). The overall shape of the cAFM-current spectrum is qualitatively well reproduced. Especially is our RN model accurately reproducing the position of the high-conductivity peaks found at the DW corners (i.e., for $\varphi = 94^\circ$, 219° , and 347°). By comparison, we estimate the proportionality constant $\sigma_0 \approx 1 \text{ S cm}^{-1}$.

The model, however, does not account for the relative heights between different peaks. The conductivity in the region $100^\circ < \varphi < 180^\circ$ is generally overestimated, therefore also the peak at $\varphi = 90^\circ$ is not well resolved. It is difficult to account for peak heights and to achieve a reasonable quantitative agreement for several reasons. First, the DWs are modeled here as a network of linear, ohmic resistors neglecting any nonlinear components that might contribute to the electronic DW transport (for instance hopping transport or charge carrier diffusion, and also not electron-hole pair recombination^[34]). Also, any spurious leakage currents across the samples' bulk or along DWs were not taken into account.

On the other hand the cAFM-measurement of the current is strongly dependent on the contact between tip and sample and might be influenced by sample surface contamination. Additionally the injection of charge carriers into the DW depends on the near-surface inclination of the DW, where large inclination angles are clearly fostering charge carrier injection. Finally one has also to consider the uncertainty from the CSHG-measurement of the DW inclination angle.

The tip-to-plate network conductivity spectrum may also be compared to the DW inclination angles at the top surface. After interpolation on a square lattice with $N = 200$ of the DW inclination angle data, the data points of the upper ten lines (in z -direction) of the lattice are plotted in **Figure 7** in comparison to the tip-to-plate-network conductivity spectrum. A good agreement in the peak positions can be seen. Also, the relative heights

Table 2. Results for the network resistivity depending on different boundary conditions for the DW state before and after sample tuning.

Boundary condition	$\rho_{pp} [\sigma_0^{-1}]$	$\rho_{tp} [\sigma_0^{-1}]$
Before tuning	1366	26923
After tuning	191	603

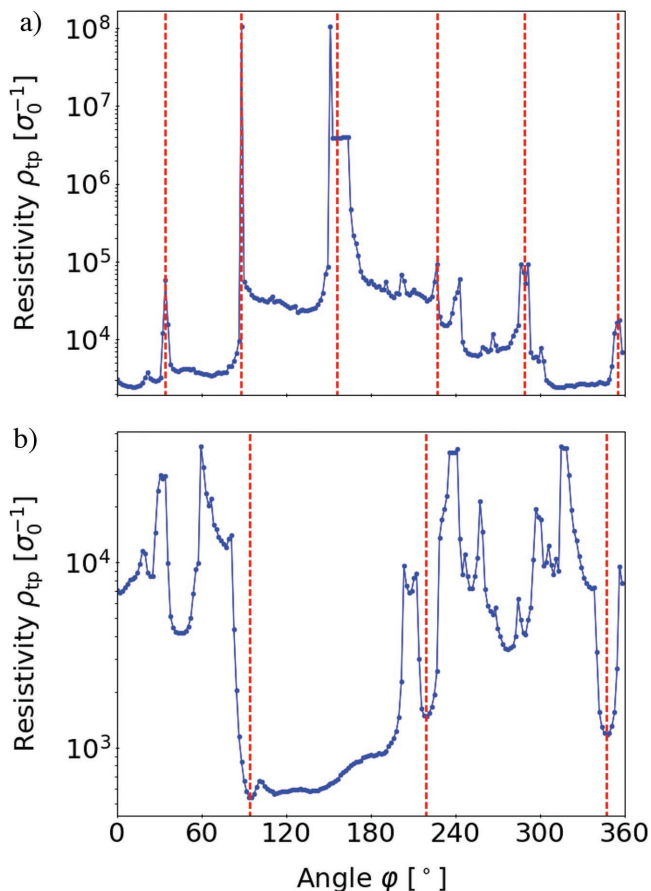


Figure 6. Network resistivity for the tip-to-plate boundary condition, calculated when scanning the tip electrode over all φ -angles. a,b) The situation before and after sample tuning, respectively. A comparison with Figure 5 shows that the edges of the DW are reflected by high-resistivity peaks at angle 34° , 88° , 156° , 227° , 289° , and 355° before DW tuning and by minima at angles 94° , 219° , and 347° afterward. See the red vertical dashed lines.

between the different peaks in the tip-to-plate-spectrum are adequately well reflected, even though the conductivity in the region $100^\circ < \varphi < 180^\circ$ again is overestimated, as is the peak at 95° . We see that the DW inclination close to the sample surface at $z = 200 \mu\text{m}$, where the major drop in the potential distribution happens, plays an important role. Nevertheless, the tip-to-plate network conductivity is determined by the whole DW inclination angle distribution. The good qualitative agreement justifies the assumption that the local resistivity of the domain wall is entirely dependent on local domain wall inclination.

4. Conclusion

In summary, we showed that electrical transport along ferroelectric DWs in lithium niobate can be well modeled by applying the concept of a RN. The RN delivers a clear connection between domain wall inclination angles (serving as the input) and the local conductivities in these DWs. More specifically, a qualitative correlation between the calculated network conductivity and the DW current spectrum measured with

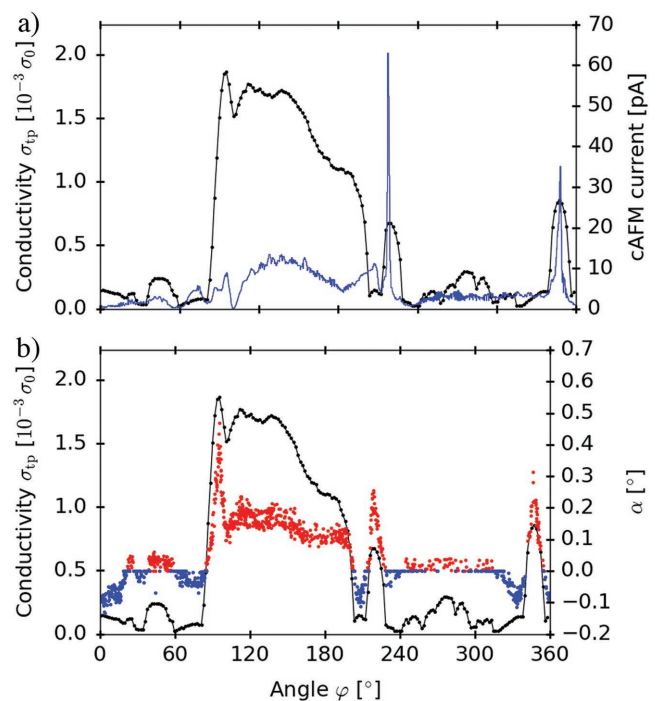


Figure 7. a) Comparison of the tip-to-plate conductivity spectrum (black), calculated by means of the resistor network approach, with the cAFM-current plotted in blue. b) Comparison of the tip-to-plate conductivity spectrum to the DW inclination angles at the samples top side (red and blue). The experimental data for both plots are the same as published by Godau.^[17]

an AFM tip on the sample surface was obtained. This allows comparing our simulations directly to experimental results, recorded using conductive atomic force microscopy. It is also a justification for the assumption of the local resistivity being entirely dependent on local domain wall inclination.

We believe that applying the RN to model electrical transport in DWs provides a strong tool for gaining a lot of insights at the mesoscopic length scale. Notably, the RN model can be easily extended to account also for time-dependent and AC-limited conductivity, for nonlinear transport regimes as well as spurious bulk conductivity. The network of Ohmic resistors then simply needs to be substituted e.g. by simple RC-units, site-specific hopping amplitudes would be introduced and simulations would have to be carried out in 3D.

Acknowledgements

Financial support by the Australian Research Council (ARC) through Discovery Grants and Future Fellowships, the German Research Foundation DFG within the cluster of excellence “Center for Advancing Electronics Dresden (cfaed)” and the research grant HA 6982/1-1, the German Academic Exchange Service DAAD and the Studienstiftung des Deutschen Volkes is gratefully acknowledged.

Conflict of Interest

The authors declare no conflict of interest.

Keywords

domain wall conductivity, ferroelectrics, network simulation, resistor model, resistor network

Received: June 7, 2017

Revised: September 26, 2017

Published online:

-
- [1] *Topological Structures in Ferroic Materials*, (Ed: J. Seidel), Springer International Publishing, Cham, Switzerland **2016**.
- [2] L. M. Eng, J. Fousek, P. Günter, *Ferroelectrics* **1997**, 191, 211.
- [3] M. Foeth, A. Sfera, P. Stadelmann, P.-A. Buffat, *J. Electron. Microsc.* **1999**, 48, 717.
- [4] Y. Daimon, Y. Cho, *Appl. Phys. Lett.* **2007**, 90, 192906.
- [5] G. Catalan, J. F. Scott, A. Schilling, J. M. Gregg, *J. Phys. Condens. Matter* **2007**, 19, 022201.
- [6] S. Farokhipoor, C. Magén, S. Venkatesan, J. Íñiguez, C. J. M. Daumont, D. Rubi, E. Snoeck, M. Mostovoy, C. de Graaf, A. Müller, M. Döblinger, C. Scheu, B. Noheda, *Nature* **2014**, 515, 379.
- [7] R. Xu, J. Karthik, A. R. Damodaran, L. W. Martin, *Nat. Commun.* **2014**, 5, 3120.
- [8] H. Chaib, T. Otto, L. M. Eng, *Phys. Status Solidi B* **2002**, 233, 250.
- [9] D. A. Allwood, G. Xiong, C. Faulkner, D. Atkinson, D. Petit, R. P. Cowburn, *Science* **2005**, 309, 1688.
- [10] G. Catalan, J. Seidel, R. Ramesh, J. F. Scott, *Rev. Mod. Phys.* **2012**, 84, 119.
- [11] J. Seidel, L. W. Martin, Q. He, Q. Zhan, Y.-H. Chu, A. Rother, M. E. Hawkrige, P. Maksymovych, P. Yu, M. Gajek, N. Balke, S. V. Kalinin, S. Gemming, F. Wang, G. Catalan, J. F. Scott, N. A. Spaldin, J. Orenstein, R. Ramesh, *Nat. Mater.* **2009**, 8, 229.
- [12] J. Guyonnet, I. Gaponenko, S. Gariglio, P. Paruch, *Adv. Mater.* **2011**, 23, 5377.
- [13] D. Meier, J. Seidel, A. Cano, K. Delaney, Y. Kumagai, M. Mostovoy, N. A. Spaldin, R. Ramesh, M. Fiebig, *Nat. Mater.* **2012**, 11, 284.
- [14] T. Sluka, A. K. Tagantsev, P. Bednyakov, N. Setter, *Nat. Commun.* **2013**, 4, 1808.
- [15] M. Schröder, A. Haußmann, A. Thiessen, E. Soergel, T. Woike, L. M. Eng, *Adv. Funct. Mater.* **2012**, 22, 3936.
- [16] M. Schröder, X. Chen, A. Haußmann, A. Thiessen, J. Poppe, D. A. Bonnelli, L. M. Eng, *Mater. Res. Express* **2014**, 1, 035012.
- [17] C. Godau, T. Kämpfe, A. Thiessen, A. Haußmann, L. M. Eng, *ACS Nano* **2017**, 11, 4816.
- [18] M. Y. Gureev, A. K. Tagantsev, N. Setter, *Phys. Rev. B: Condens. Mater. Phys.* **2011**, 83, 184104.
- [19] E. A. Eliseev, A. N. Morozovska, G. S. Svechnikov, V. Gopalan, V. Y. Shur, *Phys. Rev. B: Condens. Mater. Phys.* **2011**, 83, 235313.
- [20] B. Sturman, E. Podivilov, M. Stepanov, A. Tagantsev, N. Setter, *Phys. Rev. B: Condens. Mater. Phys.* **2015**, 92, 214112.
- [21] Y. Nakajima, P. Syers, X. Wang, R. Wang, J. Paglione, *Nat. Phys.* **2015**, 12, 213.
- [22] M. Mayr, A. Moreo, J. A. Vergés, J. Arispe, A. Feiguin, E. Dagotto, *Phys. Rev. Lett.* **2001**, 86, 135.
- [23] M. M. Parish, P. B. Littlewood, *Nature* **2003**, 426, 162.
- [24] O. Levy, D. J. Bergmann, *Phys. Rev. B: Condens. Mater. Phys.* **1992**, 46, 7189.
- [25] L. Wang, M. Yin, J. Jaroszynski, J.-H. Park, G. Mbamalu, T. Datta, *Appl. Phys. Lett.* **2016**, 109, 123104.
- [26] V. Cheianov, V. Falko, B. L. Altshuler, I. L. Aleiner, *Phys. Rev. Lett.* **2007**, 99, 176801.
- [27] R. Marshall, *Comput. J.* **2010**, 53, 644.
- [28] A. Haussmann, P. Milde, C. Erler, L. M. Eng, *Nano Lett.* **2009**, 9, 763.
- [29] A. Haußmann, A. Gemeinhardt, M. Schröder, T. Kämpfe, L. Eng, *Langmuir* **2017**, 33, 475.
- [30] T. Kämpfe, P. Reichenbach, M. Schröder, A. Haußmann, L. M. Eng, T. Woike, E. Soergel, *Phys. Rev. B: Condens. Mater. Phys.* **2014**, 89, 035314.
- [31] T. Kämpfe, P. Reichenbach, A. Haußmann, T. Woike, E. Soergel, L. M. Eng, *Appl. Phys. Lett.* **2015**, 107, 152905.
- [32] A. O'Hagan, T. Leonard, *Biometrika* **1976**, 63, 201.
- [33] S. Kirkpatrick, *Rev. Mod. Phys.* **1973**, 45, 574.
- [34] P. Maksymovych, M. Pan, P. Yu, R. Ramesh, A. P. Baddorf, S. V. Kalinin, *Nanotechnology* **2011**, 22, 254031.